Modelling the nonlinear system performance of hybrid-electric propulsion systems with aerothermodynamic interdependencies

Jan Goeing[1,*], Lucas Hanisch[2], Sebastian Lück[1], Markus Henke[2], Jens Friedrichs[1]

[1]Institute of Jet Propulsion and Turbomachinery, Technische Universitaet Braunschweig, Hermann- Blenk- Straße 37 38108, Braunschweig, Germany
[2]Institute for Electrical Machines, Traction and Drives, Technische Universitaet Braunschweig, Hans-Sommer-Str. 66 38106, Braunschweig, Germany

Abstract

The development of commercial aircraft with hybrid-electric propulsion systems is currently a subject of extensive research in order to improve local air quality and reduce combustion emissions. Among the various types of engines being studied, the two-spool parallel hybrid-electric turbofan engine is particularly challenging due to the low-pressure compressor (LPC). The hybridisation process tends to throttle the LPC, accentuating its significance in the propulsion system. For reliable operation of such systems, accurate predictions of the LPC performance during time-sensitive manoeuvres such as a go-around are important. These manoeuvres are heavily influenced by time-dependent effects that govern the propulsion system's performance. Often, the aerothermodynamic interplay between these effects is overlooked in propulsion models.

In this study, the influence of these aerothermodynamic interdependencies on the modelling results is investigated. To investigate these aerothermodynamic interactions, a dynamic model is developed to simulate the performance of the hybrid-electric turbofan engine. In comparison, a constant mass flow model is used, which is not able to simulate these interdependencies.

The results show that the aerothermodynamic interdependencies significantly affect the modelled time-resolved performance, especially for surge margin of the LPC, with this effect becoming more pronounced at higher levels of hybridisation. Therefore, the study recommends the adoption of dynamic simulation methodologies for hybrid-electric engines to guarantee high simulation precision, enhance reliability, and satisfy safety standards.

Introduction

The performance of the aircraft is directly and inseparably linked to the performance capability of the propulsion system. For this reason, continuous efforts are made to improve the power-to-weight ratio (Kappler, 1981) and ensure high reliability and efficiency for long-term aircraft operation (Wensky et al., 2010). These continuous requirements ultimately result in engine architectures that operate ever closer and with smaller margins to the aerodynamic, thermal, and structural limits of the various engine components. Furthermore, the turbofan engine plays a significant role in future aviation (Mistry et al., 2016; Bowman et al., 2018; Sahoo et al., 2020). The parallel hybrid-electric turbofan engine, as illustrated in Figure 1, poses a significant challenge to the thermal
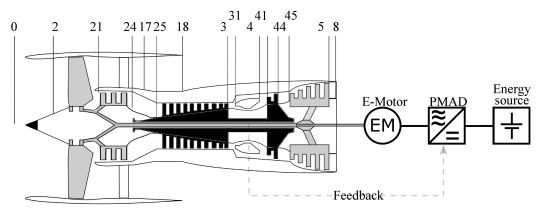
Figure 1. Schematic diagram: parallel hybrid-electric turbofan engine.

cycle due to its combination of electric power and gas turbine to drive the low-pressure spool. Due to the availability of robust measurement technology and the thrust proportionality, the N_1 speed is often used as a control variable and is used to control the electric motor (Bauerfeind, 2013). The electric motor particularly assists during takeoff and is switched off at low loads (Seitz et al., 2018; Thomas et al., 2018).

The significant limits on the performance of turbofan engines are determined by the material characteristics of the high-pressure turbines (HPT) (Boyce, 2012) and by the distance to the stability limit (surge margin, SM) of the high-pressure compressor (HPC) (Gravdahl and Egeland, 2012). In addition, the hybridisation of a conventional turbofan engine results in a higher load of the low-pressure compressor (LPC). Hence, the operation line of the LPC of a parallel hybrid-electrical turbofan engine is relocated closer to the LPC stability line (Thomas et al., 2018). To ensure safe operation of the turbofan engine, it is of utmost importance that the limits of their performance are not exceeded even under extreme conditions, such as rapid power increases in emergency situations. During such time-dependent manoeuvres, the unsteady behaviour of the engine performance is characterised by an increase in aerodynamic loads, which is attributed to various factors, primarily the inertia of rotating components and secondary effects such as heat transfer, material expansion, and gas dynamics (Walsh and Fletcher, 2004).

During the process of transitioning an aircraft engine from one steady-state operating point to another, it is achieved by means of manipulating the thrust lever position. By increasing the thrust demand, an acceleration is induced through the engine's the electronic engine control (EEC) which increases fuel flow, thereby increasing temperatures in the combustion chamber (CC). Initially, the high-pressure turbine (HPT) downstream of the CC experiences an energy overflow, while the high-pressure compressor (HPC) upstream is throttled by the temperature increase. Due to the inertia of the rotating components, which transfer energy from the HPT to the HPC, initially no increase in rotational speed is observed during acceleration due to the power imbalance, but primarily leads to a shift of the operating point of the HPC towards the stability limit due to the increased back pressure (primary effect). This reduces the core mass flow and, together with the increased fuel flow, leads to a rapid increase in the fuel to air ratio (FAR) and temperature in the combustor. This example shows that there are aerothermodynamic interdependencies between the operating performance of the components. Meanwhile, unsteady secondary effects also affect the system performance. Heat fluxes are caused by the discrepancies between material and gas temperatures, while the volume storages in the gas path are filled and emptied with gas in a time-dependent manner. The interaction of the secondary effects with the aero- and thermodynamics determines the overall system performance.

The nonlinear and time-dependent system performance motivates the investigation and numerical modelling of the parallel hybrid-electric turbofan engine in this work. Although the influence of primary and secondary effects of the engine has been sufficiently explored (Fiola, 1993; Walsh and Fletcher, 2004; Rick, 2013; Kurzke and Halliwell, 2018), the aerodynamic interdependencies of these effects on each other are only inadequately investigated. This leads to the following research question:

What is the extent of the influence of aerothermodynamic interdependencies of unsteady secondary effects on performance-specific and safety-relevant quantities?

To answer this question, the time-dependent performance of a parallel hybrid-electric turbofan engine is simulated. For this purpose, two different approaches are used: (1) the constant-mass flow (CMF) method and (2) a

dynamic approach. In this study, the dynamic approach is able to consider the aerothermodynamic interdependencies. Therefore, the parallel hybrid-electric turbofan engine and its associated performance models will be briefly introduced at the beginning of this study. Following that, the aerothermodynamic interdependencies will be defined and the impact of other secondary effects such as heat transfer on these interdependencies will be analysed. Lastly, the impact of hybridisation will be considered and the results are summarised in the conclusion.

Methods

In this study, the International Aero Engines V2500-A1 is used, which is operated on the A320-200 Figure 1 shows the schematic sectional view of the V2500-A1 engine and its corresponding stations. N_1 and N_2 are the rotational speed of the two spools of the engine, a bypass ratio of approximately 5.4 and an overall pressure ratio of up to 35.8. The maximum takeoff thrust that can be achieved is 111 kN. The architecture includes a 163 cm diameter fan downstream of the inlet diffuser (Station 2), which discharges through the secondary nozzle (Station 18), where it expands to the static ambient pressure p_0, and also directs it further through the core engine (Station 21). The fan is driven by a five-stage LPT (up to Station 5) along with the three-stage LPC (up to Station 24). The HPC (up to Station 3) has 10 stages and is connected to a two-stage HPT (up to Station 45). The complete gas expansion to the static ambient pressure p_0 occurs in the primary nozzle (Station 8). Fuel is supplied at Station 4 into an annular combustor. In Figure 2 the takeoff operation point is shown. In diagrams (a) and (b), the pressure and temperature are depicted across miscellaneous stations (Goeing et al., 2023). The calculations are based on a total mass flow rate of 360 kg/s and a fuel flow of 1.15 kg/s.

Hybridisation and electric machine

Due to the hybridisation of the N_1 shaft, less fuel flow is required for the same thrust. On the one hand, the HPC thus operates at lower mass flows and pressure ratios. On the other hand, the speed of the LP- system is kept constant, so the LPC is throttled by the lower mass flows of the HPC. Based on this, only 1 and 2 MW electric machine (EM) will be investigated (Schuchard et al., 2023).

The power management and distribution (PMAD) system, responsible for distributing power to electrical equipment such as controls, inverters, and cables, is modelled at a constant efficiency of 97%. The efficiency of the electric machine in converting from electrical to mechanical energy is plotted against speed N and torque τ in a characteristic map. This is given in Figure 3 for an EM with a maximum continuous power of 1 MW.

The EM designed by means of a finite element method is of a 9-phase design and has a power density of 6.86 kW/kg. The total weight of the electrical machine is 145.7 kg. The 9 phases are divided into three 3-phase systems each, which are necessary for the torque generation. The redundant design increases the reliability of the electrical machine because failures in one of the three 3-phase systems, which according to He et al. (2014) can account for up to 66% of the total faults, can be compensated for by the other two 3-phase systems. The main cause of the failures is due to increased partial discharge activity (Hanisch and Henke, 2022). The electric machine can basically be operated at all operating points within the characteristic diagram in Figure 3. In the control strategy presented here is operated at maximum torque τ which is available depending on the current
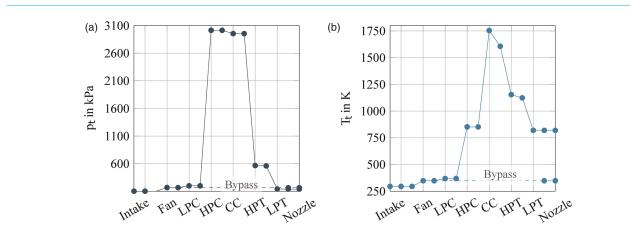

Figure 2. Pressures and temperatures within the turbo components at the takeoff operating point of the conventional aircraft engine.
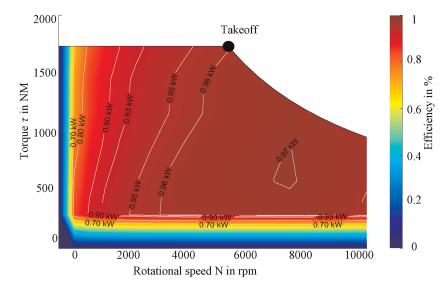
Figure 3. Efficiency of the electric machine as a function of torque and speed.

speed in order to provide maximum electrical support. Therefore, the design of the electric machine focuses on high efficiency under full load. To investigate the effects of different levels of electrical support, a second electric machine with 2 MW is being developed. The increased power is achieved by geometrically scaling the second machine at constant voltage and current density. The total weight of the 2 MW machine is 256.7 kg. The axial length increases by 19% from 218.1 mm to 259.6 mm and the diameter increases by 23% from 357.7 mm to 438.7 mm.

It should be noted that the parallel hybrid-electric architecture is a complex system and requires a multi-disciplinary approach for accurate analysis. The interaction between the conventional engine and the electric motor, as well as the PMAD system, must be considered. Furthermore, the electrical components' impact on the engine's performance, fuel consumption, and emissions must be evaluated. This necessitates the development of sophisticated mathematical models that can capture the system's dynamic behaviour, as well as the aerothermal and mechanical characteristics of the various components.

Unsteady propulsion performance simulation

In general, the equations of motion are used to model the performance of aircraft engine as well as the temporal and spatial aerothermodynamic properties in the gas path and the system behaviour of the solid components. The equations of motion are divided into the continuity, momentum, and energy equations (Liepmann and Roshko, 2001). The focus of the modelling is on the overall system performance, which considers only the 1D flows in the gas path. The system of differential equations 1 describes the conversation of mass, momentum, and energy with the cross-section A, density ρ, velocity u, internal energy E, pressure p as well as the bleed mass flow $\dot{m}_{\text{bleed}}$, momentum F and the heat flux $\dot{Q}$.

$$\frac{\partial}{\partial t} \begin{pmatrix} A\rho \\ \rho A u \\ A E \end{pmatrix} + \frac{\partial}{\partial x} \begin{pmatrix} \rho A u \\ \rho A u^2 + A p \\ u(A E + A p) \end{pmatrix} = \begin{pmatrix} -\dot{m}_{\text{bleed}} \\ F \\ \dot{Q} \end{pmatrix} \tag{1}$$

Due to the complexity of the equations of motion, various numerical approaches are used to solve the differential equation system. In general, the methods can be classified into stationary and unsteady models. The unsteady models can also be divided further into transient and dynamic methods. Essentially, transient effects are observed on time scales of seconds to minutes, while gas dynamics are on the order of milliseconds (Garrard, 1995). For the unsteady performance simulation, a steady-state initial point is required. Therefore, an iterative process, based on the constant-mass-flow (CMF) method is used (Kurzke and Halliwell, 2018; Goeing et al., 2023). The unsteady performance of the parallel hybrid-electric turbofan engine is simulated with a dynamic approach and the transient CMF method.

Dynamic model

Based on the governing equation system 1, an ordinary differential equation system is spatially discretised (see Equations 2–6), which represents the quasi 1D gas path and describes the dynamic approach Sugiyama et al. (1989). The component characteristics are included via the surface forces F_P and F_T. The pressure ratio π and efficiency η are imposed on the compressor and turbine volumes, while the burner efficiency and pressure losses are imposed on the combustor volume. The energy and momentum contributions of gravitational forces have been neglected and the frictional shear stress tensor is replaced by the Fanning and Darcy friction coefficient λ. The values in the control volumes are described with the incoming $(.)_{\text{in}}$ and outcoming $(.)_{\text{out}}$ values.

$$\frac{d}{dt}(\rho) = \frac{1}{V}(\dot{m}_{\text{in}} - \dot{m}_{\text{out}}) \tag{2}$$

$$\frac{d}{dt}(\dot{m}) = \frac{1}{L} \cdot (A_{\text{in}} \cdot p_{\text{in}} - A_{\text{out}} \cdot p_{\text{out}} + p \cdot (A_{\text{in}} - A_{\text{out}}) + \dot{m}_{\text{in}} \cdot u_{\text{in}} - \dot{m}_{\text{out}} \cdot u_{\text{out}} + F_{\text{pt}})$$
$$- \rho \frac{\lambda}{D} \cdot \frac{u^2}{2} \cdot A \tag{3}$$

$$F_{\text{pt}} = \frac{A_{\text{in}} + A_{\text{out}}}{2} \cdot (p_{\text{out}} - p_{\text{in}}) + \dot{m}_{\text{in}} \cdot (u_{\text{out}} - u_{\text{in}}) \tag{4}$$

$$\frac{d}{dt}(\rho \cdot h_t - p_t) = \frac{1}{V}(\dot{m}_{\text{in}} \cdot h_{t,\text{in}} - \dot{m}_{\text{out}} \cdot h_{t,\text{out}} + F_{Tt} + \dot{Q}) \tag{5}$$

$$F_{Tt} = \dot{m}_{\text{in}} \cdot (h_{t,\text{out}} - h_{t,\text{in}}). \tag{6}$$

Furthermore, the heat flux between components and gas path are characterised by the $\dot{Q}$ in Equation 6. The $\dot{Q}$ represents the heat transfer rate per unit time and depends on the product of surface area S, the convective heat transfer coefficient α and the difference between wall temperature T_w and gas temperature T (Li et al., 2022). In this study, only heat fluxes in the control volumes of the combustion chamber, HPT and LPT are considered:

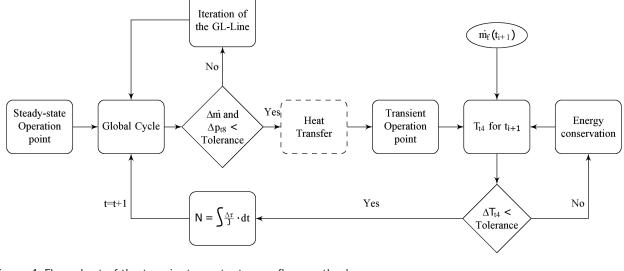$$\dot{Q} = S \cdot \alpha \cdot (T - T_w) \tag{7}$$

Finally, the change in rotational speed is determined based on the applied torques of the turbines τ_T and compressors τ_C and the moment of inertia J. Furthermore, the EM supports the turbines:

$$\frac{dN}{dt} = \frac{1}{J} \cdot (\tau_C - \tau_T - \tau_{\text{EM}}) \tag{8}$$

This system was implemented in MATLAB/-Simulink 2019a. The ordinary differential equation system is solved using a variable-order method, which sets the time step with a relative tolerance of $1 \cdot 10^{-6}$.

Constant mass flow method

The transient CMF method is illustrated by the flowchart in Figure 4. Based on a steady-state operation point, a global cycle process calculation is performed. In contrast to the steady-state CMF method, an imbalance between the compressor and turbine torque is allowed (Palmer and Cheng-Zhong, 1985; Kurzke and Halliwell, 2018) to compute the change in rotational speed (see Equation 8). The iteration variables are varied until the steady state continuity equation and expansion conditions are satisfied within the time step. The momentum equation is not included. Once the steady state target functions have converged, the transient operating point is reached, and the rotational speeds for the next time step are integrated from the time-dependent power difference. The new time step is initiated by changing the fuel flow $\dot{m}_f$. The corresponding turbine entry temperature (TET) is iterated by energy conservation within the combustor. The operating point at time t is not dependent on time $t - 1$, except

Figure 4. Flow chart of the transient constant mass flow method.

for the iterated TET and integrated rotational speeds, which are used as input parameters for the global iteration process for the next time step. No length-specific quantities are required, making it a 0D method. A time step study was conducted for the CMF methods, which showed convergence at $dt = 0.001$ s.

Based on the energies in the gas path and materials, the heat fluxes and thus the temperatures are updated after each iteration (Walsh and Fletcher, 2004). Thus, the information is not fed back during one iteration and does not affect the transient cycle process. Compared to the dynamic approach, aerothermodynamic interdependencies within the gas path as well as with the entire thermodynamic cycle are not taken into account.

The performance maps of the components are used form Goeing et al. (2020) and the models are validated in Goeing et al. (2021). Although the methods access the same gas tables, performance maps and correction models, parameter errors exist due to the different solution approaches. This maximum parameter error is 0.2% (Lück et al., 2022).

For further use, the surge margin SM between surge line SL and the operating point OP at constant rotational speed is defined as follows (Kurzke and Halliwell, 2018):

$$\mathrm{SM} = \left(\frac{\pi_{\mathrm{SL}}}{\pi_{\mathrm{OP}}} \cdot \frac{\dot{m}_{\mathrm{OP}}}{\dot{m}_{\mathrm{SL}}} - 1 \right)_{N=\mathrm{const.}} \tag{9}$$

The deviation δ between the dynamic approach and the CMF-method is calculated as follows:

$$\delta = \frac{x_{\mathrm{CMF}} - x_{\mathrm{Dynamic}}}{x_{\mathrm{Dynamic}}} \cdot 100\%. \tag{10}$$

Results and discussion

A fuel flow signal is defined and implemented as an input signal in the transient and dynamic model to investigate the aerothermodynamic interdependencies. The manoeuvre involves slam acceleration and deceleration between 11 kN and 103 kN. The fuel flow signal is shown in Figure 5a. The conventional aircraft engine is shown in blue, connected to a 1 MW EM in green and a 2 MW EM in purple. Based on hybridisation, the aircraft engine with the 2 MW motor requires the least amount of fuel during takeoff. The fuel supply is increased between 0.1 s and 1.6 s and decreased between 6.1 s and 7.6 s (dashed line).

Furthermore, Figure 5b illustrates the operating strategy of the electric motor. It is switched on at 30% of the maximum thrust (using N_1 rotational speed as a substitute value) during the manoeuvre to support the gas turbine in takeoff and increases power P_{EM} up to maximum thrust with maximum torque (see Figure 3). The strategy is oriented towards Thomas et al. (2018).
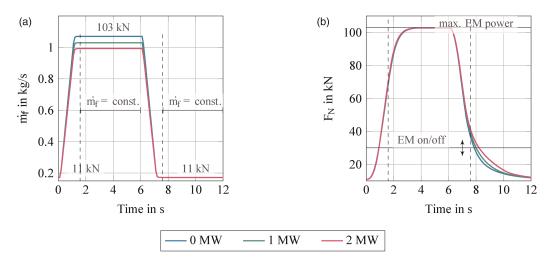
Figure 5. (a) Definition of the fuel flow signal; (b) relationship between thrust F_N and motor power P_M.

Aerothermodynamic interdependencies

Firstly, this section explains the aerodynamic interdependencies that exist in a conventional aircraft engine. For this purpose, the CMF method is compared to the dynamic approach, with a particular focus on the HPC without hybridisation and heat flux. Figure 6a shows the predicted time-dependent operating line. The dashed blue line represents the dynamic approach, while the blue solid line shows the CMF method. The curves are presented in the HPC performance map, which depicts the black speed curves in terms of pressure ratio π over corrected mass flow rate $\dot{m}_{corr.,HPC}$. It can be observed that the dynamic approach is below the CMF method during acceleration and above during the deceleration. This can be attributed to the volume storage effect that is taken into account by the dynamic model (Hashmi et al., 2021). The system responds more slowly due to volume storage, resulting in a flattening of the operational line.

In Figure 6b the deviations δ of π in dark blue, $\dot{m}$ in blue and SM in light blue between the dynamic and CMF-model are shown. Furthermore, the time points of the extreme values of the FAR are marked with the solid black line. It can be observed that the maximum deviations appear between the solid and dashed lines in the acceleration and at the black line in the deceleration. Furthermore, the deviations increase up to 3% (Q4) in pressure, 5% (Q4) in mass flow rate and decrease until −8% (Q1) in the SM. The deviations are greater during acceleration than during deceleration. Particularly noticeable is that the impact of system inertia increases up to
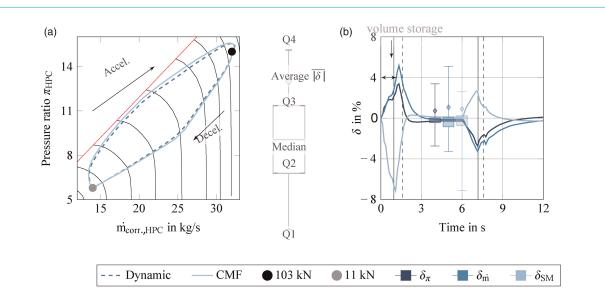

Figure 6. Numerical comparison of the HPC operating line. Left: operating line simulated by the dynamic approach and the CMF method. Right: deviation of the pressure ratio, mass flow and SM between the dynamic approach and the CMF method.

the maximum FAR, and thus is not solely responsible for the maximum deviations that occur after the solid black line.

The impact of the volume storage effect on the cycle process is particularly evident in the case of the FAR, which is shown in Figure 7a for the different components over time. The profiles demonstrate that the results of the dynamic model have significantly higher FAR in the combustor (FAR_4), high-pressure turbine (FAR_{41}), and low-pressure turbine (FAR_{45}), than the results of the CMF method. The direct influence of volume storage reduces the mass flow rate during acceleration. This reduction in mass flow rate increases the FAR. This aerothermodynamic interdependence is only captured by the dynamic model, resulting in the CMF method predicting a smaller FAR (see magnification). Furthermore, the relative deviations of FAR_4, FAR_{41} and FAR_{45} of are shown in Figure 7b. As expected, the different variations of the FAR behave similarly and are significantly influenced by the core mass flow.

Figure 8 illustrates the process of fuel mass flow rate changes, using the example of control volumes of the turbines and the entire cycle process within one time step. Changing the fuel flow leads to a new T_{t4}, which in turn changes the pressure, density, and mass flow rate due to the equations of motion and the ideal gas law. This also affects the entire cycle process, leading to changes in FAR and operating point.

These aerothermodynamic interdependencies become significantly more complex due to further secondary effects. Using heat transfer as an example, this section illustrates how the heat fluxes $\dot{Q}$ change between the gas and wall material due to a change in the fuel mass flow rate. The heat flux, in turn, interacts with the wall temperature. A new wall temperature, in turn, leads to a new heat flux and a new gas temperature (yellow circles in Figure 8). This gas temperature also affects the control volume of the turbines and influences the operating point. This impact of the heat flux will be investigated in the next section.

Heat fluxes

To advance the exploration of aerothermodynamic interdependencies, the convective heat transfer within the turbines of an aircraft engine, specifically between the gas path and materials is considered. For this purpose, the same surrogate models and correlations for discs, blades, and housings are used in the CMF method and in the dynamic model (Stephan et al., 2019; Li et al., 2022). In Figure 9a, the temperature profiles of the miscellaneous components are shown, while the box plot of relative temperature deviations is displayed in Figure 9b. The results of the deviation between the CMF and dynamic model with heat convection are illustrated in yellow and compared to the box plots from the previous subsection without heat fluxes in the same figure in blue. The temperature profiles can be qualitatively divided into temperatures upstream and downstream of the combustor. The predicted temperatures of both methods simulate qualitatively comparable profiles. The largest discrepancies are visible in T_{t5}, due to the largest heat flux. In the box plot of Figure 9b, the difference between the two T_{t5} values is particularly evident, and the modelled heat fluxes are the cause of the discrepancies. On the one hand,
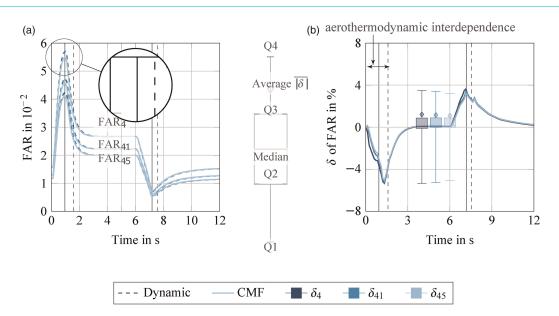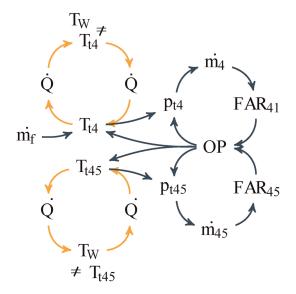

Figure 7. Numerical comparison of FAR. Left: FAR simulated by the dynamic approach and the CMF method. Right: deviation of the FAR between the dynamic approach and the CMF method.

Figure 8. Aerothermodynamic Interdependence during a time step inside the turbines.

the heat flux dampens the discrepancies, with the range of deviations (Q1 until Q4) without heat flux being 5% and with heat flux being 3%. On the other hand, the box width (Q2 until Q3) and average $|\bar{\delta}|$ increase significantly. Similar trends can be observed for T_{t4}. and T_{t45}, with the box shape of T_{t4} approaching that without heat convection. This damping effect depends on the heat fluxes, which are strongest in the LPT. Moreover, it becomes apparent that the mean deviations in the entire cycle process increase due to the aerothermodynamic interdependencies. This effect leads to a significant increase in the compressor's temperature, particularly noticeable in the LPC, whose temperature deviation range (Q1 until Q4) increases from 0.7% to 2.1%.

Level of hybridisation

In this section the influence of hybridisation on the aerothermodynamic interdependence is examined in this section without heat transfer. For this purpose, the operating strategy shown in Figure 5b is used and connected to the 1 MW or 2 MW motors (see Figure 3). Due to the hybridisation of the aircraft engine, the LPC represents a critical component. The performance is examined more closely in Figure 10. In Figure 10a, the unsteady operating line during the manoeuvre of the LPC can be seen. The conventional aircraft engine without an
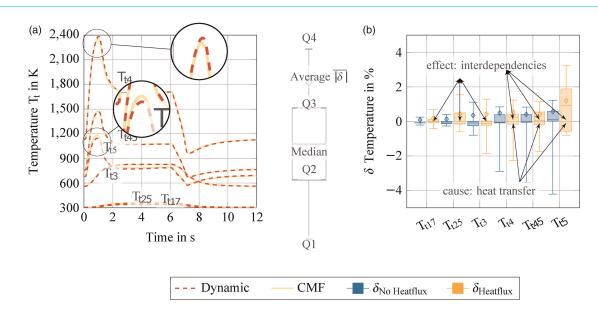

Figure 9. Numerical comparison of temperatures with and without heat flux. Left: temperatures simulated by the dynamic approach and the CMF method. Right: deviation of the temperatures between the dynamic approach and the CMF method.
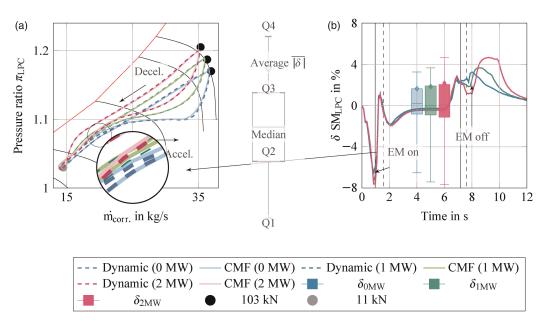
Figure 10. Impact of hybridisation on the LPC. Left: operating line during the transient manoeuvres of different aircraft configurations. Right: deviation of the SM_{LPC} between the dynamic approach and the CMF method.

electric motor is represented in blue, with 1 MW hybridisation in green, and with 2 MW in purple. The dynamic model is shown with the dashed lines and the CMF method with the solid lines. The diagram shows that the steady-state operating points are throttled at 103 kN by hybridisation, while the operating characteristics are identical at 11 kN (here, the EM is switched off). The use of the EM during time-dependent operation changes the unsteady operating characteristics and operates closer to the stability line. In Figure 10b, the differences of the SM between the CMF and the dynamic model are displayed. The plots exhibit a qualitatively similar behaviour. However, the box plots in the middle of the diagram demonstrate that the Q1 until Q4 and the median deviations increase due to the hybridisation. It is evident that the deviations in acceleration are particularly pronounced during engagement of the EM [also visible in the magnification of diagram (a)]. The deviations increase due to the control with the N_1 rotational speed as well as with the interaction with the HPC, which is less stressed due to hybridisation.

Finally, in Figure 11, the box plots of the deviations from the surge margin in diagram (a) as well as the thrust and rotational speeds in diagram (b) are shown. The results show the deviation with heat flux enabled for different levels of hybridisation. The deviations of the SM between the dynamic and CMF method increase in the LP-System and decrease in the HPC (see Figure 11a). This can be justified by the control strategy, as well as
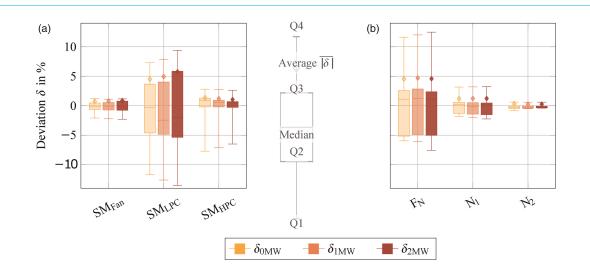

Figure 11. Numerical comparison between the dynamic approach and the CMF method with heat flux and different levels of hybridisation.

by the reduced stress on the HPC due to the hybridisation, which results in a smaller fuel flow step (see Figure 5). Furthermore, the diagram (a) shows that the LPC is most sensitive to the interactions and exhibits deviations of up to −13% (Q1). Also the aerothermodynamic interdependencies of the heat transfer increase the deviation significantly (compared to Figures 6 and 10).

The influence of the control strategy on the deviation is also visible in diagram (b). While the deviations of N_1 and the thrust increase slightly, the rational speed N_2 decreases. The quantity of thrust displays the most significant deviations, as it is an integral parameter that reacts most sensitively to the interactions.

Conclusions

In this study, the influence of aerothermodynamic interdependencies on the unsteady system performance of a hybrid-electric turbofan is investigated. Aerothermodynamic interdependencies refer to the interaction between unsteady effects, such as volume storage or heat transfer, in a time-dependent manoeuvre. Initially, the aerothermodynamic interdependencies are illustrated using a conventional turbofan engine as an example, by simulating the performance during a slam acceleration and deceleration with a dynamic approach and the constant mass flow (CMF) method. In this case, only the dynamic approach is able to model the aerothermodynamic interdependencies, while the CMF method uses steady-state conditions in the gas path. Next, heat transfer in the hot gas path is considered to increase the number of secondary effects. Finally, the system complexity is increased by the level of hybridisation with a 1 MW or 2 MW electric motor, which is engaged during the manoeuvre to support the fan at its maximum thrust. The results of the comparison can be summarised as follows:

- The volume storage effects lead to an interdependence between mass flow and fuel to air ratio, which affects the entire joule process.
- Additional secondary effects such as heat transfer can reduce the maximum discrepancies but increase the average deviations in the entire joule cycle process, especially in the low-pressure compressor (LPC).
- Hybridisation increases the load of the LPC and decreases the load of the high-pressure compressor (HPC).
- Interdependence due to the hybridisation increases the deviation of the LPC between the dynamic approach and the CMF method.

The findings of this study address the research question and conclusively demonstrate that aerothermodynamic interdependencies exert a significant impact on the time-dependent cycle processes. This influence becomes more pronounced as system complexity increases. Notably, the LPC is considerably affected by aerothermodynamic interdependencies, as evidenced by the disparities between the dynamic approach and the CMF method. Given that the LPC is a critical component in parallel-hybrid turbofan engines, the results underline the necessity of modelling these aerothermodynamic interdependencies with dynamic approaches to guarantee high simulation precision, enhance reliability, and satisfy safety standards.

Nomenclature

η	Efficiency
π	Pressure ratio
$\dot{m}$	Mass flow
$\dot{m}_f$	Fuel flow
$\dot{m}_{bleed}$	bleed flow
α	Heat transfer coefficient
τ	Torque
IFAS	Institute of jet propulsion and turbomachinery
IMAB	Institute for electrical machines, traction and drives
EGT	Exhaust gas temperature
$\dot{Q}$	Heat flux
T	Temperature
$(.)_t$	Total
t	Time
p	Pressure
BPR	Bypass ratio
N_1	Rotational speed of LP-system
N_2	Rotational speed of HP-system

CMF	Constant mass flow
SFC	Specific fuel composition
F_N	Thrust
HPC	High-pressure compressor
HPT	High-pressure turbine
LPT	Low-pressure turbine
HP	High-pressure system
LP	Low-pressure system
LPC	Low-pressure compressor
h	Enthalpy
SM	Surge margin
SL	Surge line
T_W	Wall temperature
FAR	Fuel to air ratio
OP	Operating point
S	Surface
ρ	Density
V	Volume
A	Area
λ	Darcy friction
F	Surface forces
D	Diameter
EM	E-Motor
J	Moment of inertia
L	Length
δ	Deviation
u	Velocity
E	Internal energy

Acknowledgments

Funding sources

Competing interests

Jan Goeing declares that he has no conflict of interest. Lucas Hanisch declares that he has no conflict of interest. Sebastian Lück declares that he has no conflict of interest. Markus Henke declares that he has no conflict of interest. Jens Friedrichs declares that he has no conflict of interest.

References

Bauerfeind K. (2013). Steuerung und Regelung der Turboflugtriebwerke. Basel: Springer-Verlag.

Bowman C. L., Felder J. L., and Marien, T. V. (2018). Turbo-and hybrid-electrified aircraft propulsion concepts for commercial transport. In 2018 AIAA/IEEE Electric Aircraft Technologies Symposium (EATS), IEEE. pp. 1–8.

Boyce M. P. (2012). Gas Turbine Engineering Handbook. 4th ed.. Oxford: Butterworth-Heinemann.

Fiola R. (1993), Berechnung des instationären Betriebsverhaltens von Gasturbinen unter besonderer Berücksichtigung von Sekundäreffekten, PhD thesis. Technische Universität München.

Garrard G. D. (1995). ATEC: the Aerodynamic Turbine Engine Code for the Analysis of Transient and Dynamic Gas Turbine Engine System Operations. PhD thesis, The University of Tennessee.

Goeing J., Seehausen H., Pak V., Lueck S., Seume J. R., and Friedrichs J. (2020). Influence of combined compressor and turbine deterioration on the overall performance of a jet engine using rans simulation and pseudo bond graph approach. *Journal of the Global Power and Propulsion Society*. 4: 296–308. https://doi.org/10.33737/jgpps/131109.

Goeing J., Hogrefe J., Lück S., and Friedrichs J. (2021). Validation of a dynamic simulation approach for transient performance using the example of a turbojet engine. In New Results in Numerical and Experimental Fluid Mechanics XIII: Contributions to the 22nd STAB/DGLR Symposium. Springer, pp. 559–568.

Goeing J., Seehausen H., Stania L., Nuebel N., Salomon J., et al. (2023). Virtual process for evaluating the influence of real combined module variations on the overall performance of an aircraft engine. *Journal of the Global Power and Propulsion Society*. 7: 95–112. https://doi.org/10.33737/jgpps/160055.

Gravdahl J. T. and Egeland O. (2012). Compressor Surge and Rotating Stall: Modeling and Control. London: Springer Science & Business Media.

Hanisch L. V. and Henke M. (2022). Comparison of insulation capability of round wire and hairpin windings by partial discharge measurements. In 2022 12th International Electric Drives Production Conference (EDPC). pp. 1–6.

Hashmi M. B., Lemma T. A., Ahsan S., and Rahman S. (2021). Transient behavior in variable geometry industrial gas turbines: a comprehensive overview of pertinent modeling techniques. *Entropy*. 23 (2): 250–298. https://doi.org/10.3390/e23020250.

He J., Somogyi C., Strandt A., and Demerdash, N. A. O. (2014). Diagnosis of stator winding short-circuit faults in an interior permanent magnet synchronous machine. In 2014 IEEE Energy Conversion Congress and Exposition (ECCE). pp. 3125–3130.

Kappler G. (1981). Komponentenentwicklung für energieeffiziente flugantriebe. *MTU-Berichte*. 81: 30.

Kurzke J. and Halliwell I. (2018). Propulsion and Power: an Exploration of Gas Turbine Performance Modeling. Cham: Springer.

Li Z., Li Y.-G., and Sampath S. (2022). Aeroengine transient performance simulation integrated with generic heat soakage and tip clearance model. *The Aeronautical Journal*. 126 (1302): 1265–1287. https://doi.org/10.1017/aer.2022.15.

Liepmann H. W. and Roshko A. (2001). Elements of Gasdynamics. Courier Corporation, Mineola, New York.

Lück S., Wittmann T., Göing J., Bode C., and Friedrichs J. (2022). Impact of condensation on the system performance of a fuel cell turbocharger. *Machines*. 10 (1): 59. https://doi.org/10.3390/machines10010059.

Mistry M., Koffler C., and Wong S. (2016). LCA and LCC of the world's longest pier: a case study on nickel-containing stainless steel rebar. *The International Journal of Life Cycle Assessment*. 21 (11): 1637–1644. https://doi.org/10.1007/s11367-016-1080-2.

Palmer J. and Cheng-Zhong Y. (1985). Turbotrans—a programming language for the performance simulation of arbitrary gas turbine engines with arbitrary control systems. *International Journal of Turbo and Jet Engines*. 2 (1): 19–28.

Rick H. (2013). Gasturbinen und Flugantriebe: Grundlagen, Betriebsverhalten und Simulation. Berlin Heidelberg: Springer-Verlag.

Sahoo S., Zhao X., and Kyprianidis K. (2020). A review of concepts, benefits, and challenges for future electrical propulsion-based aircraft. *Aerospace*. 7 (4): 44. 1–69. https://doi.org/10.3390/aerospace7040044.

Schuchard L., Bien M., Ziaja K., Blanken N., Göing J., et al. (2023). A study on quantitues dricing maintenance, repair and overhaul for hybrid-electric aeroengines: Gt2023-100915. In 2023 Turbomachinery Technical Conference & Exposition: ASME Turbo Expo 2023.

Seitz A., Nickl M., Stroh A., and Vratny P. C. (2018). Conceptual study of a mechanically integrated parallel hybrid electric turbofan. *Proceedings of the Institution of Mechanical Engineers, Part G: Journal of Aerospace Engineering* 232(14), 2688–2712. https://doi.org/10.1177/0954410018790141.

Stephan P., Kabelac S., Kind M., Mewes D., Schaber K., and Wetzel T. (2019.) VDI-Wärmeatlas. Berlin, Heidelberg: Springer Vieweg.

Sugiyama Y., Tabakoff W., and Hamed A. (1989). J85 surge transient simulation. *Journal of Propulsion and Power*. 5 (3): 375–381. https://doi.org/10.2514/3.23164.

The MathsWorks, Inc. (2019). Matlab and Simulink 2019a. Natick, MA..

Thomas G. L., Culley D. E., Kratz J. L., and Fisher K. L. (2018). Dynamic analysis of the hFan, a parallel hybrid electric turbofan engine. In 2018 Joint Propulsion Conference. p. 4797.

Walsh P. P. and Fletcher P. (2004). Gas Turbine Performance. Oxford, UK: John Wiley & Sons.

Wensky T., Winkler L., and Friedrichs, J. (2010). Environmental influences on engine performance degradation. In ASME Turbo Expo 2010: Power for Land, Sea, and Air. pp. 249–254.